Segmentation for Images of a Single Stem Cell Using Morphological Operations and Statistical Region Merging

Xiqiang Zheng
School of Science, Technology, Health and Humen Services,
Voorhees University,
Denmark, SC 29042, USA
xzheng@voorhees.edu

Abstract—For some images of a single stem cell, the boundary delineating the cell is discontinuous or blurry at some locations. If the statistical region merging (SRM) method is applied directly on such images, the image segmentation results may not be ideal. In this paper, for each such image, we add some gradient information into the image; then apply a discontinuous filter on the image so that the image is smoothed a bit and the edges of the image are kept well. Next, closing operations of morphology are applied on the filtered image; and the processed image is segmented using SRM. Finally, apply a threshold on the segmented image to obtain a binary image; apply a hole-filling function to the binary image; extract the biggest connected component in the hole-filled image; and apply a linear transform on the image of the biggest component to match the input image as well as possible in terms of the least squares fitting. This transformed image is the segmentation result. We have applied SRM using connectivity of 4 and 8 as well as a hexagonal lattice. The corresponding segmentation results are tabulated for convenient comparisons; and the results can show that the proposed method may be helpful for the segmentation of such images.

Keywords—image segmentation, statistical region merging, morphological operations, hexagonal sampling, image filters

I. INTRODUCTION

The usual methods and applications of image segmentation can be found in papers such as [1-18]. Deshpande et al. have shown in [15] that the statistical region merging (SRM) method yields better output than seeded region growing. As reported in [15], SRM is an effective image segmentation method for many situations. However, SRM cannot segment some images well. For example, the image of a bird shown in Table 5 in [15] is not segmented well by SRM.

For the cell images (such as those displayed at the top-left of Figs. 2-5 in this paper) shown in Examples 2 and 3 in [19] by Zade, if we apply SRM on those images directly, the segmentation results may be very bad because the boundaries of a cell may be blurry. In [19], Zade combined entropy method and some other image processing tools such as binarization and hole-filling to perform segmentation on those images. However, the computation of the entropy value on a given pixel must be based on a neighborhood region of the pixel. The image values

on the neighborhood may not represent the image value of the pixel very well. Hence, as shown at the bottom-right of Fig. 2, the boundary of the segmented image may not match the actual boundary well.

In [20] by Chudasama et al., edge detection, morphological operations and hole filling were applied for image segmentation. However, as shown in [21], the edges (produced from the edge detection) of a given object may not be connected; and hence the segmentation effect using the method in [20] for those cell images may be bad.

To overcome the deficiencies of those methods for the segmentation of those cell images, in this paper, we combine discontinuous filers, morphological operations, SRM, hexagonal lattices, thresholds, and some other image processing tools to perform image segmentation for those cell images. The segmentation results are displayed and analyzed using some efficient criteria. For those images of a single stem cell, this algorithm usually has a better image segmentation effect than the previous algorithms introduced.

II. IMAGE SEGMENTATION USING SRM AND SOME OTHER IMAGE PROCESSING TOOLS

In this section, we show the details of the image segmentation method based on filters, morphological closing operations, SRM, and thresholds for the segmentation of those cell images.

A. Discontinuous Filters

The usual Gaussian filters for image processing are smooth filters, which effectively reduce noise but also blur out the edges. For the purpose of image segmentation, the edges should be kept as well as possible while performing image filtering. In this paper, a discontinuous filter is constructed as follows.

Let $W_z = 11$ and $W_{center} = 6$. Let M be a matrix of size 11 by 11 such that $M(6,6) = 100(W_z)^2$ and $M(i,j) = 1$ if $i \neq 6$ or $j \neq 6$. Let s be the sum of all entries of M and let $h_0 = \frac{1}{s}M$. Then the sum of all entries of h_0 is 1. Because $h_0(6,6)$ is much bigger than other entries of h_0, the matrix h_0 can serve as a discontinuous image filter. Let h_g be the Gaussian filter of size 11 by 11．Finally, let $h = 0.75(h_0) + 0.25(h_g)$．Then h is

discontinuous because h_0 is discontinuous and h_g is continuous. In this paper, we use the filter h to perform image filtering such that image edges are kept well.

B. Morphological Operations and Hexagonal Lattices

Morphological operations can be found in papers such as [22-25]. Hexagonal lattices were introduced in [24-26]. In [24], an efficient algorithm for morphological operations on hexagonal lattices was developed.

Let SE_4 be the structuring represented by the 7 by 7 matrix whose elements are ones except 3 zeros at each conner of the square matrix. SE_4 can be generated by the Matlab command `strel('disk',4)`. Also let Ξ_3 be the regular hexagonal structure corresponding to the structure shown in the left side of Fig. 1 in [28] by Vince and Zheng. The detailed definitions of SE_4 and Ξ_3 can be found in [25] by Zheng. SE_4 is a structuring element for morphological operations on square lattices; and Ξ_3 is a structuring element for morphological operations on hexagonal lattices. Each of SE_4 and Ξ_3 has 37 entries that are ones. Hence, those two structuring elements can be applied to compare square lattices with hexagonal lattices fairly for the effect of morphological operations.

A morphological closing operation dilates an image with a structuring element and then erodes the dilated image using the same structuring element. The closing operation is useful for filling out small holes in an image. For any integer $k > 0$, an image can be dilated using one of the structuring elements for k times. Then the image can be eroded using the same structuring element elements for k times. The value of k can be chosen according to the segmentation effects of different kinds of images.

C. The SRM Method for Image Segmentation

In [12], the SRM method for hexagonally sampled images was implemented. In [12], the SRM method for a 2-dimensional Cartesian image with 8-connectivity was also implemented. It was shown that the hexagonal lattices or square lattices with connectivity 8 usually obtain better effect than square lattices with connectivity 4 for image segmentation using SRM. In this paper, we perform image segmentation utilizing hexagonal lattices as well as square lattices with connectivity 4 or 8.

D. Thresholds, Hole Filling, and Extracting the Biggest Connected Component

Because the segmented image from SRM may have more than two components, we need to apply a suitable threshold on the segmented image so that the final image has just two components. The threshold can be expressed as the mean value of the segmented image from SRM times a positive number, which is named as the *threshold coefficient*. The threshold coefficient should be suitably chosen to obtain good segmentation results. After the threshold, the image may have holes; and the image may consist of more than two connected components. Hence, we need to apply a hole filling function and another function extracting the biggest connected component. The final segmentation result is based on the biggest connected component.

E. Least Squares Fitting to Obatin the Final Image Segmentation Result

Because of the previous image processing steps, the values of the original input image may have been changed much. We need to apply a linear transform on the image of the biggest connected component so that the transformed image can match the input image as well as possible in terms of the least squares fitting.

F. The Detailed Steps of the Algorithm Based on Morphology and SRM

Now we show details of this algorithm. For an input image I_0 of size m_0 by n_0 by d, our algorithm consists of the following 12 steps to obtain the segmented image. To compare this algorithm with the algorithm based on entropy, we assume that $d = 1$. Let us call this algorithm *MorphSRM*.

1. Set the values for the *gradient coefficient* G_c to be used in Step 4, the *exponent index* $p > 1$ (for image processing before filtering) to be used in Step 5, the number N_{morph} of closing operations to be used in Step 8, and the threshold coefficient T_c to be used in Step 10.

2. Convert I_0 to double type; and let I be a sub-image of I_0 such that the single cell is contained in I more compactly than in I_0. For the images constituting the video in [19], we let

   $I = \{I_0(i,j) \mid 91 \leq i \leq m_0 - 390, 191 \leq j \leq n_0 - 290\}$.

3. Apply a linear transformation such that the minimal and maximal value of the transformed image to be 0 and 255, respectively. Let I_2 denote the transformed image.

4. For each pixel (i,j) of I, compute the 2-norm $\|\nabla I(i,j)\|$ of the gradient of I. Let I_g be the image defined by $I_g(i,j) = I(i,j) + G_c \cdot \|\nabla I(i,j)\|$.

5. Let I_3 be the image defined by $I_3(i,j) = \frac{4 \cdot I_g(i,j)}{255}$; and let I_4 be the image defined by $I_4(i,j) = (I_3(i,j))^p$. Because $p > 1$, this step and the next step usually make the salient features in the image more evident as shown at the top-right of Fig. 2.

6. Perform filtering on the image I_4 using the filter h. Let I_5 denote the filtered image; and let I_6 be the image defined by $I_6(i,j) = (I_5(i,j))^{\frac{1}{p}}$. Let M_6 denote the maximal value of the image I_6. Let I_7 be the image defined by $I_7(i,j) = \frac{255 \cdot I_6(i,j)}{M_6}$.

7. To apply a hexagonal lattice for image segmentation, as in [12], resample the image to a hexagonal lattice with the same sampling rate as the usual square lattice.

8. Perform the dilations for N_{morph} times using the structuring element SE_4 for the 2D Cartesian image and using the structuring element Ξ_3 for the

   hexagonally sampled image. Then perform the corresponding erosions for N_{morph} times; and let I_8

   denote the image after those operations. The value of N_{morph} depends on image size and kinds of images. For the images in this paper, we set $N_{morph} = 3$.

9. As in [12], we use 0.4 as the weight of Sobel derivative and use $g = 256$ to perform image segmentation using SRM on the square lattice (with connectivity 4 or 8) and the hexagonal lattice. In this paper, for each image, we apply SRM twice to obtain better image segmentation effect. First, we let $Q = 2^{14}$ and let 3 be the minimal size to obtain a segmented image using SRM. In the 2nd time, the segmented image is used as the input image; let 4 be the minimal size; and let $Q = 2^i$ with i taking values 12, 11, 10, 9, and 8 to perform image segmentation using SRM. Let I_{srm} denote the image after the second application of SRM.

10. Apply the threshold (introduced before) on I_{srm} to obtain the corresponding binary image I_{thrsd}.

11. As in [19], apply a hole-filling function (imfill in Matlab) on the image I_{thrsd}; extract the biggest connected component (bwpropfilt in Matlab) in the hole-filled image; and denote the resulting image as $I_{largest}$.

12. Apply a linear transformation on the image $I_{largest}$ so that the transformed image matches the input image I_2 as well as possible in terms of the least squares fitting; and denote the transformed image as $I_{segmented}$, which is the final result of the segmentation by this algorithm. Finally, as in [12], compute the *mean absolute error* (MAE) between $I_{segmented}$ and I_2.

III. EXPERIMENTAL RESULTS

For the video (stem_cell_migration.mp4) in Example 3 in [19], in Step 1 of the algorithm *MorphSRM*, we set $G_c = 1.4$, $p = 8$, $N_{morph} = 3$, and $T_c = 1.05$. We tested the first 30 frames (images) of the video, and computed the average of the corresponding 30 *MAEs* for each algorithm. For the algorithm in this paper, we applied the square lattice (with connection 4 and 8) as well as the hexagonal lattice. Then the best one among the 3 outputs is chosen to compare with the result of the algorithm based on entropy method. The *MAEs* for the segmentation of those frames are shown in Fig. 1. The average *MAEs* for the algorithm *MorphSRM* and the entropy-based algorithm are 5.6339 and 5.6743, respectively. They imply that *MorphSRM* is better than the entropy-based algorithm.

For Frame 19 of the video, the input and segmented images are shown in Fig. 2. We can see that the segmented cell from the entropy-based algorithm has a hole; furthermore, the boundary of the segmented cell is not ideal. The segmented image from *MorphSRM* is obviously better.
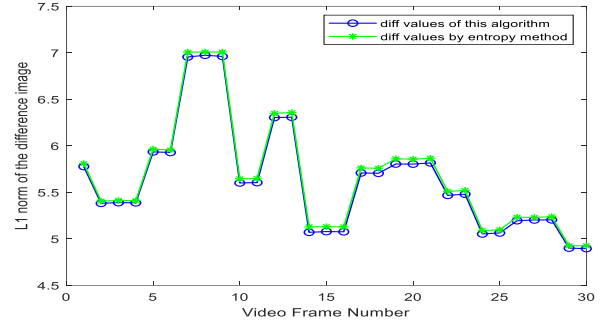

Fig. 1. The MAEs for the segmentation of the first 30 frames of the video in Example 3 in [19]. The green and the blue indicate the MAEs for the entropy-based algorithm and MorphSRM, respectively.
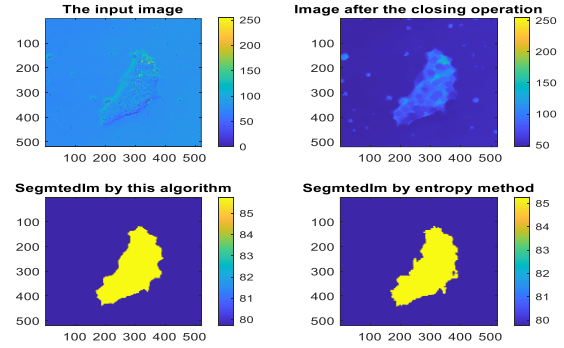

Fig. 2. The input and segmented images for Frame 19 of the video. Top-left is the input; top-right is the image after the closing operation from the input; bottom-left is the segmented image from MorphSRM; and bottom-right is the segmented image using entropy.
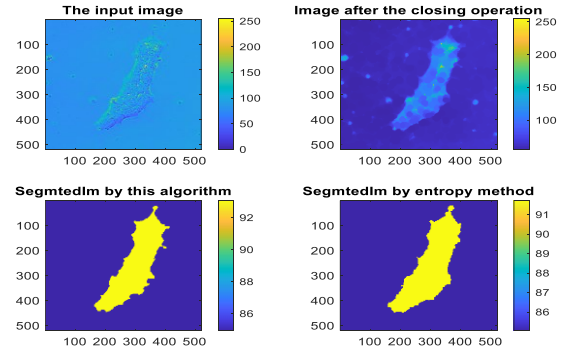

Fig. 3. The input and segmented images when $G_c = 1.4$ and $T_c = 1.05$ for Frame 20 of the video. Top-left is the input; top-right is the image after the closing operation from the input; bottom-left is the segmented image from MorphSRM; and bottom-right is the segmented image using entropy.

For a given frame, we may change the values of G_c and T_c to achieve better segmentation effect. For example, for Frame 20, the result using the original values of G_c and T_c is not very good because a few small pieces of the cell are lost as shown at the bottom-left of Fig. 3. This deficiency is remedied when $G_c = 2$ and $T_c = 1$ as shown at the bottom-left of Fig. 4.

For the image in Ex. 2 in [19], we set $G_c = 2$ and $T_c = 0.98$.

The segmented images are shown in Fig. 5. The segmented image from *MorphSRM* may provide some useful information, or may be complementary to the result from the entropy-based algorithm.

IV. CONCLUSION AND FUTURE WORK

We have developed a novel computer algorithm for the segmentation of those cell images. The algorithm is tested using some images. The experimental results are evaluated using the *MAE* measure. The segmented images are displayed, and the *MAE* values are computed for convenient comparisons. We have implemented the algorithm for the hexagonal lattice as well as the square lattice with connectivity 4 or 8. Hence, for the same input image, there are three segmented images. Those segmented images may be better than (or provide complementary information to) the segmentation results using entropy. The *MAE* values for the tested images can show that our algorithm usually performs better than the entropy-based algorithm. The segmented images using our algorithm usually do not have such default as those using entropy.
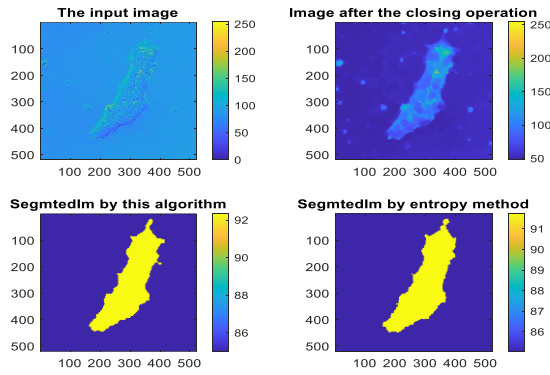

Fig. 4. The input and segmented images when $G_c = 2$ and $T_c = 1$ for Frame 20 of the video. Top-left is the input; top-right is the image after the closing operation from the input; bottom-left is the segmented image from MorphSRM; and bottom-right is the segmented image using entropy.
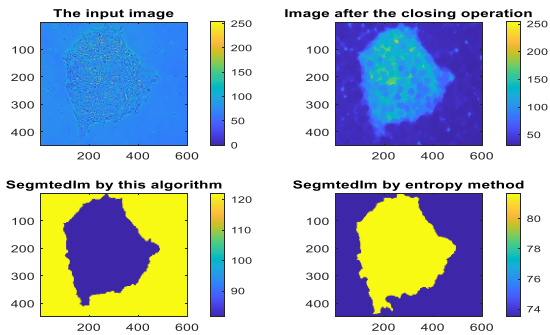

Fig. 5. The input and segmented images when $G_c = 2$ and $T_c = 0.98$ for the image in Example 2 in [19]. Top-left is the input; top-right is the image after the closing operation from the input; bottom-left is the segmented image from MorphSRM; and bottom-right is the segmented image using entropy.

Among the first 30 frames of the video, 20 of those frames achieve best segmentation results from the hexagonal lattice; and 10 of those frames achieve best segmentation results from the square lattice with connectivity 8. Hence, for the

segmentation of the stem cell images, usually the hexagonal lattice performs better than the square lattice; and for the square lattice, connectivity 8 performs better than connectivity 4. To achieve better segmentation result, the rectangular image should contain the cell as compactly as possible. Otherwise, the biggest connected component extracted in Step 11 of the algorithm may not consist of the pixels of the cell.

In the future, we may analyze the parameters in the algorithm *MorphSRM* or perform some statistics. Because image segmentation techniques continue to advance, we may compare this algorithm with some other recent works for image segmentation. We may also apply this algorithm to other application domains or to 3D images as in [27].

REFERENCES

[1] G. Windisch and M. Kozlovszky, "Framework for comparison and evaluation of image segmentation algorithms for medical imaging," IFMBE proceedings, vol. 49, pp. 480-483, 2015.

[2] M. Khani, "Medical image segmentation using machine learning," Thesis, University of Wisconsin-Milwaukee, 2021.

[3] D. Luo, W. Zeng, J. Chen, and W. Tang, "Deep learning for automatic image segmentation in stomatology and its clinical application," Front Med Technol, vol. 3, 2021.

[4] S. Minaee, Y. Boykov, F. Porikli, A. Plaza, N. Kehtarnavaz, and D. Terzopoulos, "Image segmentation using deep learning: a survey," IEEE Trans. Pattern Anal. Mach. Intell., vol. 44, no. 7, pp. 3523-3542, 2022.

[5] P. Malhotra, S. Gupta, D. Koundal, A. Zaguia, and W. Enbeyle, "Deep neural networks for medical image segmentation," J Healthc Eng, 2022.

[6] K. Otsuki, Y. Iwamoto, Y. W. Chen, A. Furukawa, and S. Kanasaki, "Cine-MR image segmentation for assessment of small bowel motility function using 3D U-Net," Journal of Image and Graphics, vol. 7, no. 4, pp. 134-139, 2019.

[7] A. O. Joshua, F. V. Nelwamondo, and G. Mabuza-Hocquet, "Blood vessel segmentation from fundus images using modified u-net convolutional neural network," Journal of Image and Graphics, vol. 8, no. 1, pp. 21–25, 2020.

[8] K. S. Nija, C. P. Anupama, V. P. Gopi, and V. S. Anitha, "Automated segmentation of optic disc using statistical region merging and morphological operations," Phys Eng Sci Med., vol. 43, no. 3, pp. 857-869, 2020.

[9] R. Nock and F. Nielsen, "Statistical region merging," IEEE Trans. Pattern Anal. Mach. Intell., vol. 26, no. 11, pp. 1452–1458, 2004.

[10] R. Gharleghi, N. Chen, A. Sowmya and S. Beier, "Towards automated coronary artery segmentation: A systematic review," Comput Methods Programs Biomed, vol. 225, Article 107015, 2022.

[11] H. Du, K. Shao, F. Bao, Y. Zhang, C. Gao, W. Wu and C. Zhang, "Automated coronary artery tree segmentation in coronary cta using a multiobjective clustering and toroidal model-guided tracking method," Comput Methods Programs Biomed, vol. 199, Article 105908, 2021.

[12] X. Zheng, "Image segmentation for hexagonally sampled images using statistical region merging," The 6th International Conf. on Imaging, Signal Processing and Communications (ICISPC), Kumamoto, Japan, published by IEEE Xplore, pp. 37-42, 2022.

[13] T. Wan, X. Shang, W. Yang, J. Chen, D. Li and Z. Qin, "Automated coronary artery tree segmentation in X-ray angiography using improved Hessian based enhancement and statistical region merging," Comput Methods Programs Biomed, vol. 157, pp. 179-190, 2018.

[14] H. Wang, Z. Shen, Z. Zhang, Z. Xu, S. Li, S. Jiao and Y. Lei, "Improvement of region-merging image segmentation accuracy using multiple merging criteria," Remote Sensing, vol. 13, no. 14:2782, 2021.

[15] A. Deshpande, P. Dahikar and P. Agrawal, "An experiment with statistical region merging and seeded region growing image segmentation techniques," In Recent Trends in Image Processing and Pattern Recognition; Santosh, K.C., Hegadi, R.S., Eds.; Springer: Singapore, pp. 493–506, 2019.

[16] G. Lee, M. Bajger, and M. Caon, "Multi-organ segmentation of CT images using statistical region merging," Proc. of the 9th IASTED International Conf. on Biomedical Engineering (BioMed 2012), pp. 199-206, 2012.

[17] X. Wang and J. Wu, "Remote sensing image segmentation based on statistical region merging and nonlinear diffusion," the 2nd Internat. Asia Conf. on Informatics in Control, Automation and Robotics (CAR 2010), pp. 32-35, 2010.

[18] M. Howes, M. Bajger, G. Lee, F. Bucci, and S. Martelli, "Texture enhanced statistical region merging with application to automatic knee bones segmentation from CT," 2021 Digital Image Computing: Techniques and Applications (DICTA), pp. 1-8, 2021.

[19] S. Zade, "Medical image segmentation," Retrieved March 27, 2023. https://www.mathworks.com/matlabcentral/fileexchange/88019-medical-image-segmentation; https://github.com/mathworks/Medical-Image-Segmentation/releases/tag/v1.0

[20] D. Chudasama, T. Patel, S. Joshi and G.I. Prajapati, "Image segmentation using morphological operations," Int. J. Comput. Appl., vol. 117, no. 2, pp. 16-19, 2015.

[21] Ur Rehman Khan and K. Thakur "An efficient fuzzy logic based edge detection algorithm for gray scale image", Int. J. Emerging Technology and Advanced Engineering, vol. 2, no. 8, 2012 .

[22] J. Serra, "Image analysis and mathematical morphology," Academic Press, London, 1982.

[23] F. Shih, "Image processing and mathematical morphology: fundamentals and applications," 1st edn. CRC Press, 2017.

[24] X. Zheng, "Some efficient algorithms for morphological operations on hexagonal lattices and regular hexagonal domains," Proc. SPIE, vol. 11584, pp. 115840B-1–9, 2020.

[25] X. Zheng, "Computer simulations for the denoising effect of morphological reconstructions for CT images on hexagonal grids and regular hexagonal regions," Proc. SPIE, vol. 12076, pp. 120760G-1–12, 2021.

[26] X. Zheng, "Rectangular body-centered cuboid packing lattices and their possible applications," J. Comput. Sci. Res., vol. 1, no. 2, pp. 1–7, 2019.

[27] X. Zheng and F. Gu, "Fast Fourier transform on FCC and BCC lattices with outputs on FCC and BCC lattices respectively," J. Math. Imaging Vis., vol. 49, no. 3, pp. 530–550, 2014.

[28] A. Vince and X. Zheng, "Computing the discrete Fourier transform on a lattice," J. Math. Imaging Vis., vol. 28, no. 2, pp. 125–133, 2007.